Applied Catalysis B: Environmental 209 (2017) 285–294

Contents lists available at ScienceDirect

Applied Catalysis B: Environmental

journal homepage: www.elsevier.com/locate/apcatb

Atomic scale g-C_3N_4/Bi_2WO_6 2D/2D heterojunction with enhanced photocatalytic degradation of ibuprofen under visible light irradiation

Jiajia Wang[a,b], Lin Tang[a,b,*], Guangming Zeng[a,b], Yaocheng Deng[a,b], Yani Liu[a,b], Longlu Wang[c], Yaoyu Zhou[d], Zhi Guo[a,b], Jingjing Wang[a,b], Chen Zhang[a,b]

[a] College of Environmental Science and Engineering, Hunan University, Changsha, 410082, PR China
[b] Key Laboratory of Environmental Biology and Pollution Control (Hunan University), Ministry of Education, Changsha 410082, PR China
[c] State Key Laboratory of Chemo/Biosensing and Chemometrics, Hunan University, Changsha 410082, PR China
[d] College of Resources and Environment, Hunan Agricultural University, Changsha, 410082, PR China

ARTICLE INFO

Article history:
Received 4 January 2017
Received in revised form 27 February 2017
Accepted 3 March 2017

Keywords:
Atomic scale
2D/2D heterojunction
Monolayer Bi2WO6
Ultrathin g-C3N4 nanosheets
Photocatalysis

ABSTRACT

Although photocatalytic degradation is an ideal strategy for cleaning environmental pollution, it remains challenging to construct a highly efficient photocatalytic system by steering the charge flow in a precise manner. In this study, a novel atomic scale g-C_3N_4/Bi_2WO_6 heterojunction (UTCB) constructed by ultrathin g-C_3N_4 nanosheets (ug-CN) and monolayer Bi_2WO_6 nanosheets (m-BWO) was successfully prepared by hydrothermal reaction. The UTCB heterojunctions were characterized by various techniques including XRD, TEM, AFM, BET measurements, UV–vis spectrometry, and XPS. The results indicated that UTCB heterojunctions were assembly of m-BWO on ug-CN and presented high separation efficiency of photogenerated carriers. Under visible light irradiation, the optimum molar ratio of ug-CN/m-BWO (1:4, UTCB-25) reached almost 96.1% removal efficiency of IBF within 1 h, which was about 2.7 times as that of pure m-BWO. The photocatalytic mechanisms of UTCB-25 were revealed, suggesting that the synergistic effect of UTCB-25 heterojunction with strong interfacial interaction promoted the photoinduced charge separation. According to the LC–MS/MS, five photodegradation pathways of IBF under visible light irradiation were proposed. This study could open new opportunities for the rational design and a better understanding of atomic scale two dimensions/two dimensions (2D/2D) heterojunctions in environmental or other applications.

1. Introduction

With the development of industry and population, energy crisis and environmental pollution have aroused people's concern [1–3]. It is widely accepted that photocatalysts are significant materials for achieving a future sustainable society with graceful environment [4–6]. However, developing photocatalyst materials that can efficiently utilize solar energy for practical application is of great technical challenge due to the limitation of photon absorption, charge separation, and charge utilization [7,8].

Recent progress in graphene studies are provoking tremendous interest in exfoliation-based fabrication of 2D single-layered nanosheets [9]. The as-exfoliated 2D monolayers with atomic thicknesses offer opportunities to the atomic-level understanding of charge separation [10–12]. Such monolayers enable atomic level control over architectures and electronic structures, thus manipulating the charge flow from the electron–hole separation sites to their surface in a desired route [13]. However, individual semiconductor monolayers still encounter substantial charge recombination for photocatalytic degradation, because they lack sufficient active sites to manipulate the fates of these surface reaching electrons [14,15]. To address this issue and also to realize the charge flow at the atomic level, it is highly desirable constructing atomic scale 2D/2D heterostructures, because its face-to-face contact might form the larger interface region as compared to the point-to-face contact in the 0D/2D heterojunction and the line-to-face contact in the 1D/2D heterojunction [16,17]. 2D/2D heterostructures have been proven to be an effective way for photodegradation of contaminants with successful cases such as SnS_2/g-C_3N_4, g-C_3N_4/$K^+Ca_2Nb_3O_{10}^-$, rGO/Bi_2WO_6, CdS/MoS_2, and $BiOIO_3$/BiOI [16,18–22]. Bi_2WO_6, with a narrow band gap about 2.7 eV, is a more promising photocatalyst, due to its stable physical and chemical properties, low cost, and non-toxicity. Bi_2WO_6 also

* Corresponding author at: College of Environmental Science and Engineering, Hunan University, Changsha, 410082, PR China.
E-mail address: tanglin@hnu.edu.cn (L. Tang).

http://dx.doi.org/10.1016/j.apcatb.2017.03.019
0926-3373/

consists of alternate stacking of $[Bi_2O_2]$ layers and perovskite-type layers with oxygen atoms shared between layers. It has been widely used in environmental remediation such as PPCPs removal [23,24], treatment of VOCs indoor [25], and reduction of carbon dioxide to the fuels [26]. Recently, Zhou et al. fabricated monolayer Bi_2WO_6 nanosheets (m-BWO) [27], in which holes are directly generated on the active surfaces and electrons in the middle layer on irradiation, leading to ultrafast charge separation. Notably, graphite-like carbon nitride (g-C_3N_4), a rising star of metal-free photocatalyst, has attracted worldwide attention due to its low cost, polymeric p-conjugated structure, and remarkable physical and chemical properties [28,29]. A large amount of ultrathin g-C_3N_4 nanosheets (ug-CN) based heterostructured photocatalysts such as $NaNbO_3$/g-C_3N_4, graphene/g-C_3N_4, Bi/g-C_3N_4 [6,30,31] has been constructed, and they exhibited a remarkably high photoactivity towards water splitting, disinfection, and NO reduction.

Motivated by the above studies, this work is to initially integrate ug-CN and m-BWO into an atomic scale 2D/2D heterostructure as an efficient visible light driven photocatalyst. We can successfully steer the charge separation, transportation and consumption all at the atomic level to construct a highly active photodegradation system. In such a system, electrons originating from visible light-irradiated ug-CN transfer to the middle $[WO_4]^{2-}$ layers, and holes photogenerated from $[BiO]^+$ layers directly transfer to intimate ug-CN nanosheets. What's more, the large specific surface area of ug-CN can increase the specific surface area of the photocatalysts, thus providing more active sites. Ibuprofen (IBF) is selected as the target PPCPs for photocatalytic removal with the as-prepared UTCB heterojunctions. As a widely used anti-inflammatory drug, IBF has been detected in surface water and wastewater in a range from ng/L^{-1} to mg/L^{-1} levels, and its stability of non-photolysis and non-biodegradation makes it accumulate in aquatic environment and sediments [32–36]. What arouses public concern is that IBF was reported to inhibit the postembryonic development of anuran species in freshwater [37].

In the present study, an atomic scale g-C_3N_4/Bi_2WO_6 2D-2D heterostructure was successfully constructed by ultrathin g-C_3N_4 nanosheets and monolayer Bi_2WO_6 nanosheets (donated as UTCB). Such atomic scale 2D-2D heterostructure provided a large contact area for fast interfacial charge separation as well as a large specific surface area. The photocatalytic performance of UTCB heterostructures was investigated by degradation of IBF under visible light irradiation. The results suggested that UTCB heterojunctions displayed much higher photocatalytic activity under visible light irradiation than bare ug-CN and m-BWO nanosheets. The possible visible light driven degradation pathway of IBF removal was investigated. The construction of atomic scale 2D-2D heterostructures with intimate contact opens new opportunities for rational design highly active visible light photocatalysts for environmental applications and other applications.

2. Materials and methods

2.1. Materials

Bismuth nitrate pentahydrate ($Bi(NO_3)_3{\cdot}5H_2O$, Aladdin, Shanghai, 99.5%), sodium tungstate dihydrate ($Na_2WO_4{\cdot}2H_2O$, Aladdin, Shanghai, 99.5%), melamine ($C_3H_6N_6$, Damao chemical reagent factory, Tianjin, 99.0%), cetyltrimethyl ammonium bromide (CTAB, $C_{19}H_{42}BrN$, Damao chemical reagent factory, Tianjin, 90.0%) were used. Scavenger stock solution used to quench reactive species were 10 mM ethylenediamine tetra acetic acid disodium salt (EDTA-Na_2) (Aladdin, Shanghai) for photogenerated-holes (h^+), 10 mM isopropanol (Aladdin, Shanghai) for hydroxyl radicals ($^{\bullet}OH$), 2 mM benzoquinone (BQ, Sigma, USA) for superoxide radical ($^{\bullet}O_2^-$). Tap water samples were collected from the Changsha water group (Changsha, China) and stored at 4 °C. River wastewater samples were collected from Xiangjiang River and stored at 4 °C. All other reagents were of analytical grade and used without further purification.

2.2. Synthesis of UTCB heterojunctions

The detailed synthesis procedure of UTCB heterojunctions was prepared by hydrothermal reaction. Firstly, the ultrathin g-C_3N_4 nanosheets were prepared according to the previously reported method [15]. Melamine was calcined at 520 °C for 4 h with the heating rate of 2.3 °C min^{-1}. After calcination, the bulk g-C_3N_4 was milled into powder and heated at 500 °C for 2 h with the heating rate of 5 °C min^{-1}. A light yellow powder of g-C_3N_4 nanosheets was finally obtained. Secondly, the ultrathin g-C_3N_4/Bi_2WO_6 heterojunction was prepared by a bottom-up approach [27]. A certain amount of as-prepared ultrathin g-C_3N_4 nanosheets, 50 mg CTAB, 1 mmol $Na_2WO_4{\cdot}2H_2O$, and 2 mmol $Bi(NO_3)_3{\cdot}5H_2O$ were added in 80 mL deionized water. After 30 min stirring, the mixed solution was transferred to a 100 mL Teflon-lined autoclave. Then the autoclave was treated at 120 °C for 24 h. Finally, the product was collected and washed several times with deionized water and dried at 60 °C in air for 10 h. The different mass ratio of ug-CN/m-BWO at 0.05:1, 0.1:1, 0.25:1, and 0.5:1 were prepared and signed as UTCB-5, UTCB-10, UTCB-25, and UTCB-50, respectively. In contrast, pure m-BWO was prepared in the same procedure without adding ug-CN.

2.3. Characterization

The phase and composition of the as prepared samples were identified by powder X-ray diffraction (XRD, Rigaku, Japan). The morphologies and microstructures of the as-prepared samples were investigated by Transmission Electron Microscopy (TEM, JEOLJEM-2100F, accelerating voltage 200 kV). UV−vis diffuse reflectance spectra of the samples were recorded on a UV–vis diffuse reflection spectrophotometer (DRS, Cary 300, USA) with $BaSO_4$ used as a reference. The surface elemental composition of the samples was analyzed by X-ray photoelectron spectroscopy (XPS, Thermo Fisher Scientific, UK). The thickness of the samples was determined by atomic force microscopic (AFM, Bioscope system, USA).

2.4. Photocatalytic degradation procedure

The as-prepared UTCB heterojunctions were utilized for photodegradation of IBF under visible light irradiation of a 300 W xenon lamp (CEL-HXF300, Beijing AuLight) with the 420 nm cutoff filter. The light spectrum and light intensity of the compacted fluorescent lamps were determined by a light monitor (International light, RPS900-R, USA), which consisted of visible light with average intensity of 326 mW cm^{-2}, and no UVA determined. Generally, 10 mg of UTCB heterojunctions and 2.5 mL of IBF solution (500 μM), were added to 50 mL of deionized water in a beaker under stirring at 400 rpm throughout the test. Before photocatalytic reaction, the suspension was stirred in the dark for 30 min to reach the adsorption/desorption equilibrium. At given time intervals, 1 mL of the suspension was collected and then filtered through 0.45 μm membrane filters for analysis. The experiments were conducted in triplicate. The concentration of IBF was analyzed by high performance liquid chromatography (HPLC, Angilent) equipped with a UV detector (SPD-10AV) and C18 column (250 mm × 4.6 mm). The mobile phase was a mixture of 80/20 (v/v) methyl alcohol-water

(pH 2.5, adjusted by phosphoric acid). The eluent was delivered at a rate of 1 mL min^{-1} and the wavelength for detection was 223 nm.

2.5. Liquid chromatography–mass spectrometry

Determination of the photodegradation intermediates of IBF were carried out on a LC–MS/MS system that consisted of a 1290 HPLC (Agilent, USA) and an API 3000 mass analyzer. The HPLC column used was a Kromasil C18 column (4.6 × 100 mm) from Angilent. Separation of the analytes was achieved by a methanol/water isocratic elution (80% methanol, 20% water), flow rate of 0.2 mL/min, injected volume of 10 μL, and column temperature at 302 K (30 °C). An electrospray interface (ESI) was used for MS–MS measurements in negative ionization mode at the full scan acquisition between m/z 100–500. The collision energy varied according to the requirements for different measurements, and the other parameters were set as the following: the ESI was done at 4 kV at temperature of 400 °C; the gas (N_2) flow rate was 11 L min^{-1}, and nebulizer was 15 psi; nitrogen was used as a collision gas at 2500 mbar.

2.6. Photoelectrochemical measurements

CHI 660C electrochemical analyzer (CHI-660C, China) in a three-electrode cell was employed to measure the photoelectrochemical responses of the samples. FTO electrodes coated by UTCB samples served as the working electrode. A Pt wire and Ag/AgCl served as counter and the reference electrodes, respectively, and 0.1 M Na_2SO_4 was used as supporting electrolyte in this system. The visible light source was provided by a 300 W Xe lamp with lighting wavelength range of 420–700 nm. All of the electrochemical measurements were carried out at room temperature.

2.7. Cycling experiments

To investigate the reusability of UTCB heterojunctions for photocatalytic removal of IBF, experiments were conducted in five consecutive cycles using UTCB-25. After each cycle of the photocatalytic reaction, UTCB-25 was separated and recycled from the solution by filtration, then washed thoroughly with deionized water to remove residual pollutants and dried in an oven at a temperature of 60 °C, and the resulting heterojunctions were used in the succeeding cycle.

3. Results and discussion

3.1. Characterizations

The crystal phase of the prepared composites was measured by XRD. As shown in Fig. 1, the distinct diffraction peaks of samples could be found at 28.3°, 32.8°, 47.1°, 56.0°, and 58.5°, which corresponded to the (1 3 1), (2 0 0), (2 0 2), (1 3 3), and (2 6 2) crystal planes of orthorhombic Bi_2WO_6 (JCPDS NO. 39-0256), respectively. The characteristic peaks of ug-CN in the samples could not be detected, because of the low crystallinity of ug-CN and overlap between the main peaks of g-C_3N_4 and Bi_2WO_6 at 27.4° [38]. The successful compositing of UTCB was confirmed by the following XPS and TEM analysis.

To get detailed characterization of the morphologies and microstructures of the samples, transmission electron microscopy (TEM) and high-resolution transmission electron microscopy (HRTEM) analysis were performed. The low and high magnification TEM images of UTCB-25 are shown in Fig. 2. Fig. 2a exhibited the synthesized m-BWO with a sheet shaped structure, in which smooth and intimate interfaces were observed between the ug-CN and m-BWO, which demonstrated the formation of ug-CN/m-BWO

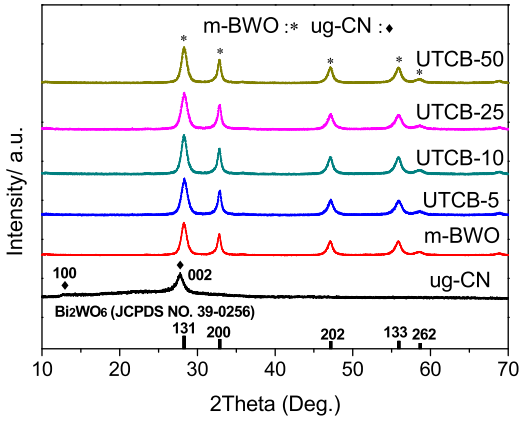

Fig 1. XRD patterns of ug-CN, m-BWO, and UTCB heterojunctions.

heterojunctions. This result also implied that UTCB-25 was heterogeneous in structure rather than a physical mixture of two separate phases of ug-CN and m-BWO. Moreover, the observed transparent nature indicated their ultrathin structures [39]. The clear lattice fringe in HRTEM (Fig. 2b) should be ascribed to m-BWO, and the d spacing value was 0.315 nm, corresponding to the (131) planes of orthorhombic-structured Bi_2WO_6 [40]. The light parts corresponded to ug-CN. The observed tight junction of interface was possibly favorable for the photogenerated carriers transfer between ug-CN and m-BWO, which promoted the separation of photogenerated electron−hole pairs.

The composition and microstructure of UTCB-25 were further investigated by high-angle annular dark-field scanning transmission electron microscopy (HAADF-STEM) and energy dispersive X-ray spectroscopy (EDS) elemental scanning (Fig. 2c). The STEM image and the EDS elemental mapping from this area displayed a homogeneous distribution of C, N, Bi, W, and O elements in UTCB-25 heterojunction. The mapping image of Bi, W, and O could be seen in the same shape. Meanwhile, it could also be observed that C and N elements originating from ug-CN nanosheets distributed evenly under the surface of m-BWO. These results demonstrated the assembly of m-BWO on ug-CN nanosheets successfully.

The atomic force microscopic (AFM) was employed to further determine the thickness of UTCB-25. The AFM images and the corresponding height histograms of the nanosheets are presented in Fig. 3a and b. The corresponding height profiles (Fig. 3b) demonstrated that the average thickness values of the small-sized nanoflakes was about 0.8 nm, well-matching with the theoretical ones of the m-BWO monolayers [27]. The relatively large nanosheet with the height of 1.7 nm and the width of 400 nm was ug-CN, because the width of m-BWO ranged from 20 to 180 nm according to the TEM image (Fig. 2a). This result was also consistent with the TEM image in Fig. S1 which demonstrated the presence of this kind of hetero-self-assembled structure. AFM images further evidenced the assembly of m-BWO on ug-CN.

The optical absorption of ug-CN, m-BWO, and UTCB heterojunctions was analyzed based on the UV–vis diffuse reflection spectrophotometer. As shown in Fig. 4a, m-BWO showed an adsorption edge of 450 nm, corresponding to a band gap of approximately 2.68 eV, and m-BWO has a band gap of approximately 2.69 eV (inset of Fig. 4a). In contrast with pure m-BWO, when ug-CN content in the UTCB heterojunctions increased, all heterojunction samples showed enhanced absorption in the visible light range the absorption accompanying a red shift in the absorption edge. The bandgap energy of UTCB-25 was ca. 2.63 eV (inset of Fig. 4a), which was lower than that of the m-BWO by 0.05 eV. The above results can be ascribed to the synergetic effect between m-BWO and ug-CN interface, which improved the separation and transfer of

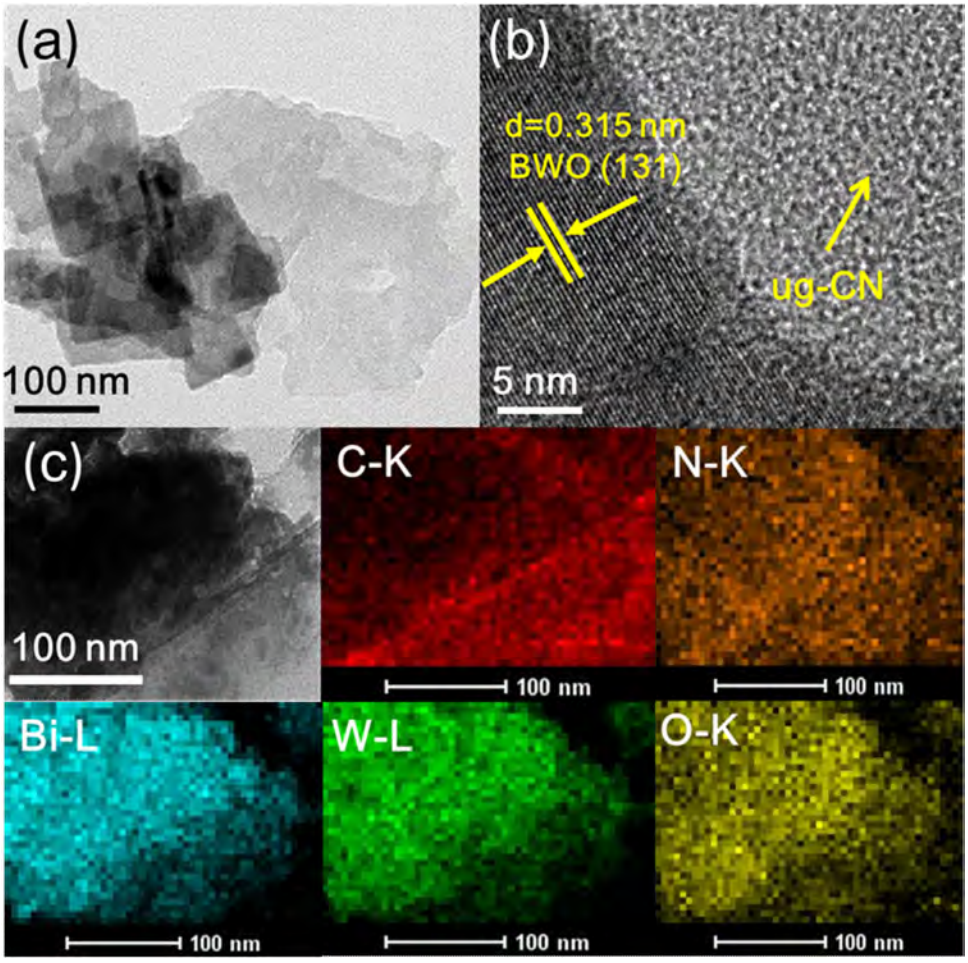

Fig. 2. TEM and HR-TEM images of (a, b) UTCB-25; and c) HAADF-STEM image and the corresponding EDS elemental mapping images of the UTCB-25 heterojunction.

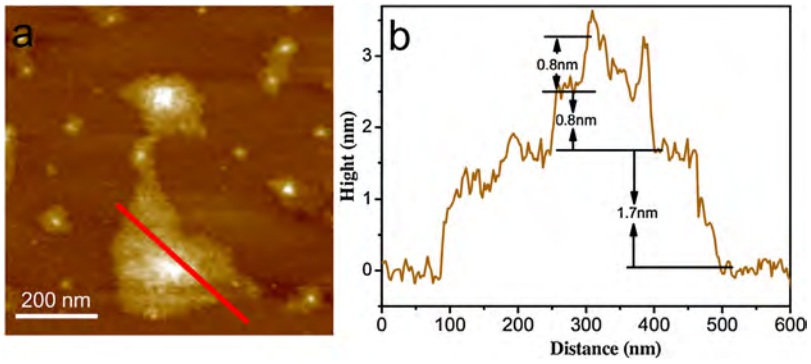

Fig. 3. a) AFM image; and b) cross-section profile of UTCB-25.

photogenerated carriers and resulted in a higher photocatalytic activity of these heterojunctions. The XPS VB spectra were employed to investigate the band structure of ug-CN and m-BWO. According to the result, the positions of valence band of ug-CN and m-BWO are found to be at 1.55 and 0.36 eV (Fig. 4b), respectively. According to the equation of $E_{CB} = Eg - E_{VB}$, the conduction band edges of ug-CN and m-BWO are calculated to be −1.14 and −2.32 eV, respectively. The data in Fig. 4b indicate that ug-CN and m-BWO have suitable band potential to construct a hetero-junction structure.

The surface chemical compositions and states of UTCB-25 were further investigated by X-ray photoelectron spectroscopy (XPS). Chemical binding energies were observed at approximately 288.2, 398.8, 35.2, 164.7, and 529.8 eV which can be attributed to C 1s, N 1s, W 4f, Bi 4f, O1s (shown in Fig. 5a), respectively. It implied that the composite contains C, N, W, Bi, and O. From the XPS spectra of Bi 4f (Fig. 5b), the two peaks at approximately 159.4 and 164.7 eV can be assigned to the binding energies of Bi 4f7/2 and Bi 4f5/2, respectively. The peak located at 529.8 eV is attributed to O 1s (Fig. 5c). Two peaks located at 35.2 and 37.4 eV are assigned to W4f (Fig. 5d). As shown in Fig. 5e, C 1s peak at about 284.2 eV can be assigned to graphitic carbon or adventitious carbon and also the sp2-hybridized of C—N. The peak at around 288.2 eV is attributed to sp2-hybridized C of N—C=N in the aromatic ring of the g-C_3N_4

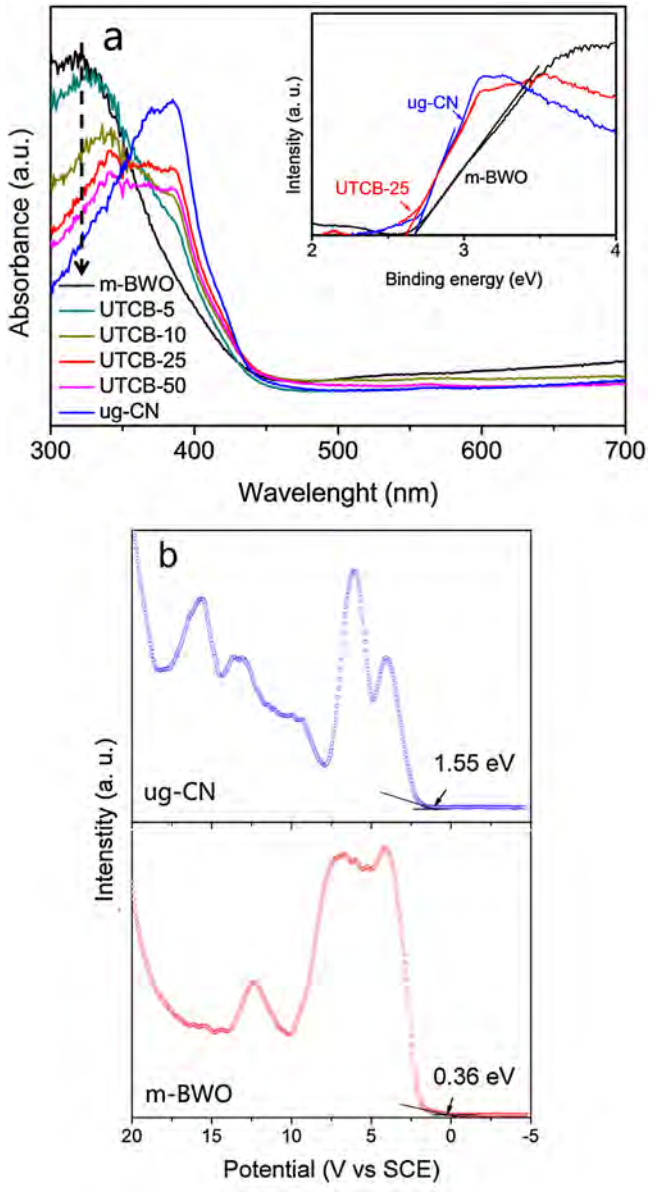

Fig. 4. a) UV–vis spectra of pure ug-CN, m-BWO, and UTCB heterojunctions; b) VB XPS spectra of ug-CN and m-BWO.

[38]. The N 1s peaks in Fig. 5f could be fitted into three peaks at ~398.8, 400.5, and 403.9 eV, corresponding to the sp2 bonded nitrogen in the form of C—N=C, the tertiary nitrogen (N-$(C)_3$) groups, and the surface uncondensed amino groups (C—N—H), respectively [41]. The above discussion confirms the existence of ug-CN in the UTCB-25 heterojunction.

Fig. 6 illustrates the nitrogen adsorption–desorption isotherms and the pore size distributions by BJH method for m-BWO, UTCB-5, and UTCB-25. It could be seen that the nitrogen adsorption–desorption isotherms of these five samples were similar and all of them possess a type IV isotherm and a type H3 hysteresis loops according to the IUPAC classification [42], indicating the presence of mesoporous structure. The BET specific surface areas and pore volumes of UTCB heterojunctions were summarized in Table S1. As listed in Table S1, the BET specific surface area (S_{BET}) of m-BWO is about 29.4 $m^2\ g^{-1}$. With increasing the ug-CN content, the S_{BET} of the sample becomes larger. The S_{BET} of UTCB-25 is 42.2 $m^2\ g^{-1}$.

Table 1
The parameters of the tap water and river water from Xiang River.

Samples	NH_3-N/mg L^{-1}	COD/mg L^{-1}	Cl^-/mg L^{-1}	NO_3^-/mg L^{-1}	TOC/mg L^{-1}
Tap water	0.016	1.31	0.65	0.64	0.64
River water	0.211	3.86	0.084	0.91	2.26

3.2. Photocatalytic performance of UTCB hybrid heterojunctions

3.2.1. Optimization of UTCB hybrid heterojunctions

The photocatalytic activity of the as-prepared UTCB heterojunctions was evaluated through the photocatalytic degradation of IBF under visible light irradiation. Pure m-BWO and ug-CN were also used for comparison. As shown in Fig. 7a, the degradation of IBF was negligible without any catalyst, suggesting no photolysis occurred for IBF during 1 h of light irradiation. Only about 38.2% degradation occurred in the presence of pure ug-CN, while almost 67.3% degradation occurred with pure m-BWO under the same experimental conditions. Excitingly, the present results further showed that UTCB-25 presented a much higher efficiency (~96.1%) than that of pure m-BWO and ug-CN for IBF degradation through a pseudo first-order kinetic reaction. It is probably due to that the ug-CN helped the separation of photogenerated carriers, thus enhancing photocatalytic degradation efficiency of IBF by the UTCB heterojunctions. What's more, according to the adsorption experiment results (shown in Fig. S2), the adsorption of IBF increased with the increase of the loading amount of ug-CN, because the large specific area of ug-CN enlarged the specific area of UTCB heterojunctions. Obviously, UTCB-25 had the highest photocatalytic degradation efficiency with a rate constant of 0.052 min^{-1} for IBF removal, which was about 2.7 times as that of pure m-BWO as 0.020 min^{-1} (Fig. 7b). Therefore, UTCB-25 was chosen as the optimum photocatalyst in the following experiments. However, as the mass ratio of ug-CN further increased to 1:2, the photocatalytic activity of UTCB-50 then decreased, though the adsorption ability for IBF of UTCB-50 was the highest. It is probably due to that the large amount of ug-CN covered the active sites of m-BWO. To study the total organic carbon (TOC) quantification during photocatalytic removal of IBF by UTCB-25, TOC was measured with a Shimazu TOC analyzer (TOC-VCPH). As shown in Fig. S3, about 21.8% of TOC was removed after a 1 h reaction, and nearly 78.1% removal was achieved after 4 h, suggesting that the IBF mineralization by the UTCB composites is possible.

3.2.2. Effect of water matrix

Considering the real water application, the water matrix is an important parameter. The effect of various water sources for the removal of IBF using UTCB-25 is shown in Fig. 8a. After 1 h of photocatalytic reactions, degradation efficiencies of about 96.1%, 75.3%, and 38.2% were achieved in IBF-obtained deionized water, tap water, and river water, respectively. Obviously, degradation rate of IBF in river water was the lowest. The inhibition of the photocatalytic activity of UTCB-25 under visible light irradiation in natural water matrix was likely due to the consumption of reactive species by natural organic matter (NOM) [43,44]. As shown in Table 1, both tap water and river water contained relatively high TOC. It can be shown that NOM expressed by TOC (2.26 mg L^{-1} of river wastewater) might be the main competitor of IBF for the generated reactive species [45]. Nevertheless, UTCB-25 could still remove most of the IBF with a prolonged irradiation time of 2 h in river wastewater, indicating its promising practicality for water purification.

It is well-known that bicarbonate ions, chlorine, and sulfate are the most common anions in natural water, and most of them existed as the form of salts. Furthermore, the electrolytes could influence the photocatalytic reaction in practical wastewater application. Herein, $NaHCO_3$, NaCl, and Na_2SO_4 were used to investigate

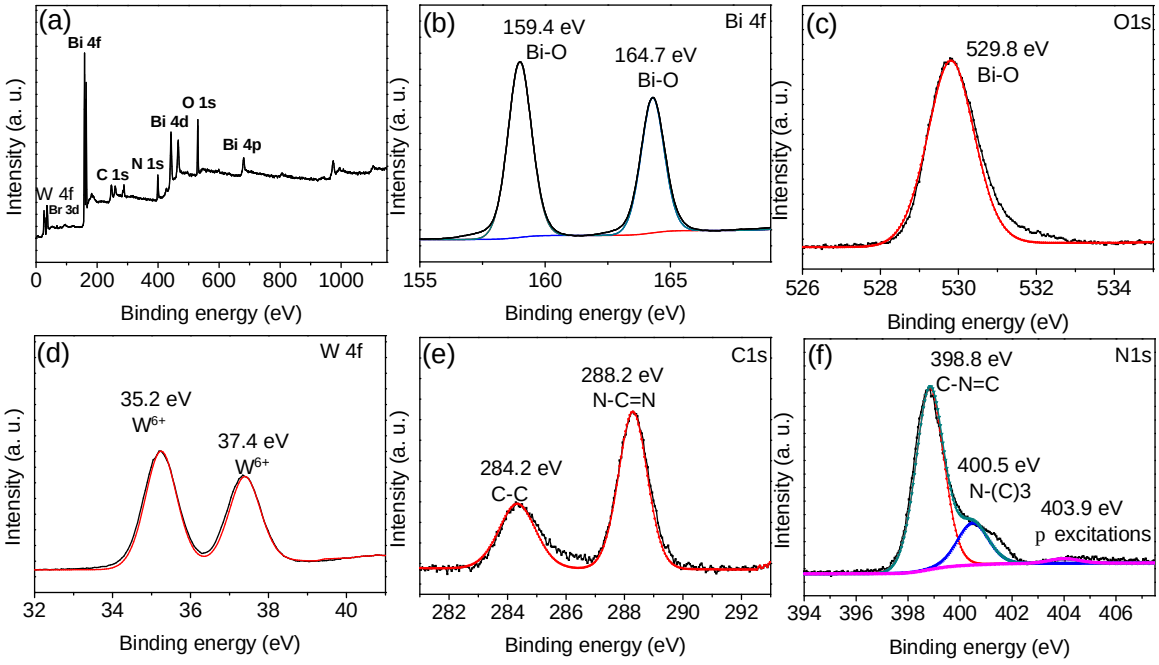

Fig. 5. XPS spectra of UTCB-25: a) survey spectrum; b) Bi 4f spectrum; c) O 1 s spectrum; d) W 4f spectrum; e) C 1s spectrum; f) N spectrum.

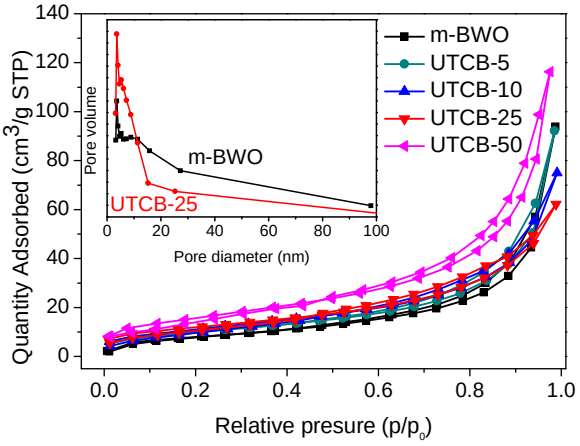

Fig. 6. N_2 adsorption-desorption isotherm of m-BWO and UTCB heterojunctions.

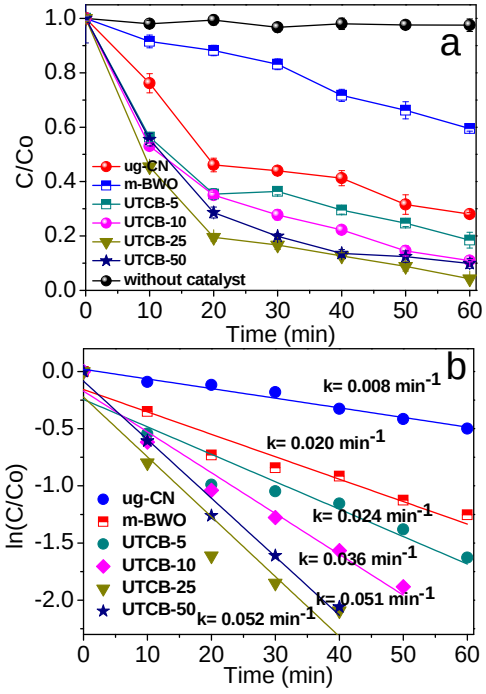

Fig. 7. a) Photodegradation of IBF by using pure ug-CN, m-BWO, and UTCB heterojunctions under visible light irradiation; b) Plots of $\ln(C/C_0)$ vs irradiation time. [IBF] = 25 μM; [UTCB] = 0.2 g L^{-1}.

the detailed effects on the photocatalytic degradation of IBF by UTCB-25 heterojunction. Fig. 8b displayed the results of IBF removal in the presence of the above electrolytes at a concentration of 5 mM, and the corresponding removal rates decreased in the order as follows: NaCl > Na_2SO_4 > $NaHCO_3$. A slight inhibition could be found within the NaCl electrolyte, but the difference was insignificant. The decrease in the photodegradation of IBF might be ascribed to the competitive adsorption between Cl^- and IBF on the surface of the catalyst [27]. However, obvious negative effects were found in the presence of Na_2SO_4 and $NaHCO_3$ on the photocatalytic degradation of IBF. According to previous report [46], bicarbonate and sulfate ions are the scavengers of •OH radical. Bicarbonate also acts as h^+ scavenger. The equations are given as follows:

$$SO_4^{2-} + {}^{\bullet}OH \rightarrow {}^{\bullet}SO_4^- + OH^- \quad (1)$$

$$HCO_3^- + {}^{\bullet}OH \rightarrow {}^{\bullet}CO_3^- + H_2O \quad (2)$$

$$HCO_3^- + h^+ \rightarrow {}^{\bullet}CO_3^- + H^+ \quad (3)$$

In the above reactions, SO_4^{2-} and HCO_3^- could react with the generated reactive species to form sulfate radicals ($^{\bullet}SO_4^-$) and carbonate radicals ($^{\bullet}CO_3^-$). Especially, $^{\bullet}CO_3^-$ is a weaker oxidizing agent [47]. It took a longer time for $^{\bullet}SO_4^-$ and $^{\bullet}CO_3^-$ to react with IBF than h^+ in theory, thus retarding the IBF decay rate.

3.2.3. Photodegradation intermediates of IBF

The main photodegradation intermediates were identified by LC–MS/MS to determine the reaction mechanism along the degradation route. A total of 8 aromatic intermediates were tentatively identified in the solution (see Table S2). At the beginning of reaction

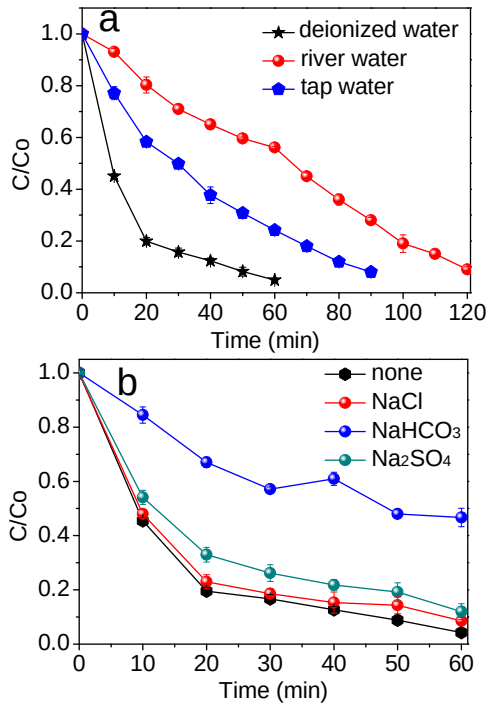

Fig. 8. a) Photocatalytic degradation of IBF in deionized water, tap water and river water under visible light irradiation; b) Effect of supporting electrolyte on the degradation of IBF by UTCB-25 under visible light irradiation. [IBF] = 25 μM; [UTCB-25] = 0.2 g L^{-1}; All electrolytes at a concentration of 5 mM.

(Fig. S4a), IBF can be directly observed at *m*/*z* 205. No intermediate was detected during the first 30 min adsorption process (Fig. S4b). The main intermediates emerged in Fig. S4c. The intensity of IBF peak decreased during the photodegradation process, whereas some main intermediates with *m*/*z* of 238, 221, and 178 were generated after 30 min irradiation. The intermediates were produced in hydroxylation process and followed by decarboxylation. The process could be presented by pathway III, IV, and V (Fig. 9). This result is consistent with the previous reports that •OH radicals' attack can occur at various positions of ibuprofen to yield a variety of hydroxylated IBU [48,49]. Besides, the intermediates with smaller *m*/*z* (162, 133) were also found, because h^+ attacked the hydroxylated ibuprofens which resulted in decarboxylation at the ibuprofen side chains. These products were produced by direct decarboxylation (pathway I in Fig. 9). The direct decarboxylation was the main degradation pathway of IBF. Besides, it is also proposed that IBF would directly lose $C_3O_2H_3$ (pathway II in Fig. 9). As the reaction continued, the deprotonated IBF molecular iron with *m*/*z* = 205 almost disappeared after 1 h (Fig. S4d). These results demonstrated that the intermediates engendered in the photocatalytic degradation were degraded in succession after a period of photodegradation time.

From a practical application point of view, reuse of materials is a very important economical factor in many water treatment processes. To evaluate the reusability of the UTCB-25, the heterojunction were separated and recycled from the solution by filtration separated and reused for four successive photocatalytic degradation cycles of IBF. As shown in Fig. S5, the degradation efficiency of IBF after each cycle was measured to be about 96.1%, 95.4%, 94.8%, 94.5%, and 93.7% for 1st, 2nd, 3rd, 4th, and 5th run, respectively. The result indicated that UTCB-25 is durable and stable in the photocatalytic degradation of IBF. The structural stability of recycled UTCB-25 was further examined by XRD analysis after the fifth run. As shown in Fig. S6, compared with the fresh UTCB-25, no obvious change in the XRD pattern was found for the recycled sample, suggesting its good crystal stability.

3.3. Photocatalytic mechanisms of UTCB-25 hybrid heterojunction

3.3.1. Photocurrent intensity

To obtain the transient photo-response of ug-CN, m-BWO, and UTCB-25, photocurrent density were measured under

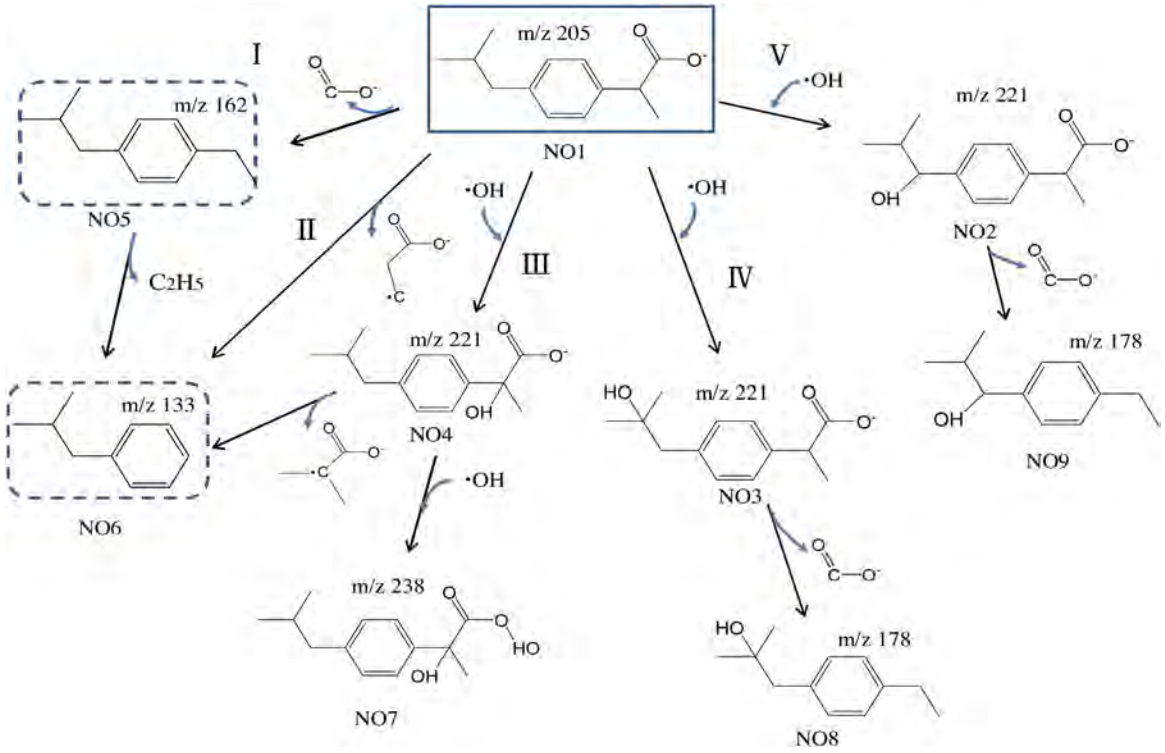

Fig. 9. The proposed photocatalytic degradation pathway of IBF.

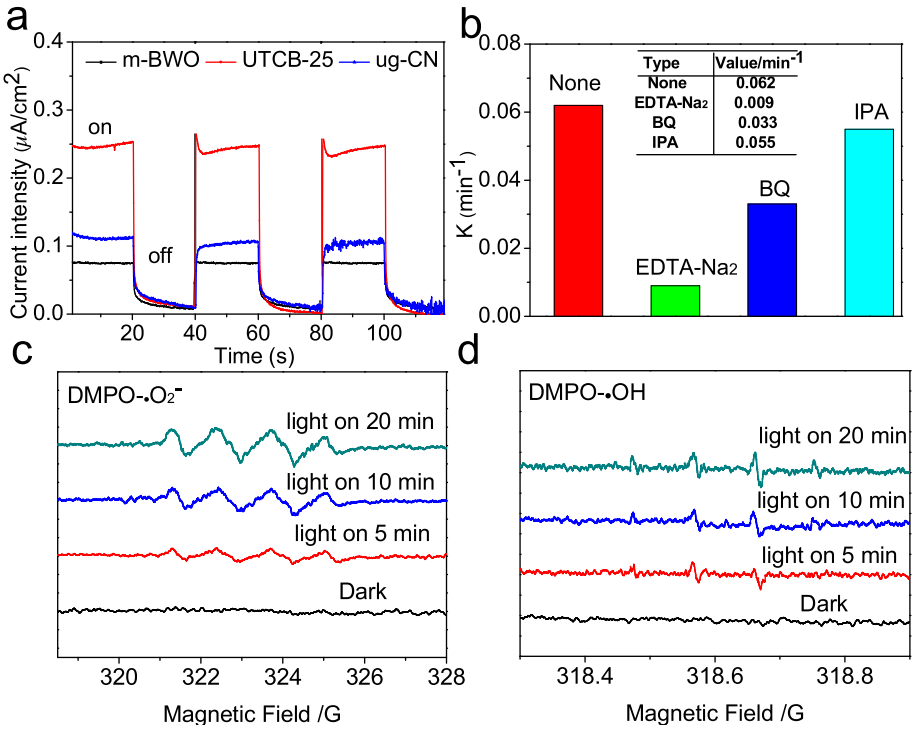

Fig. 10. a) Transient photocurrent response of pure ug-CN, m-BWO, and UTCB-25 visible light visible light irradiation; b) Photodegradation efficiency of IBF on UTCB-25 by addition of addition of 2 mM benzoquinone, 10 mM isopropanol, 10 mM EDTA-Na_2; [IBF] = 25 μM; [UTCB-25] = 0.2 g L^{-1}; c) ESR spectra of radical adducts trapped by DMPO (•O_2^- and •OH) in UTCB-25 dispersion in the dark and under visible light irradiation in methanol dispersion for DMPO-•O_2^-; d) in aqueous dispersion for DMPO-•OH.

illumination with several cycles of 20 s interval light on or off in 0.5 M Na_2SO_4 solution. Larger photocurrent indicated a separation efficiency of higher electrons and holes. As illustrated in Fig. 10a, it was worth noticing that the photocurrent density of UTCB-25 composite electrode (0.25 μA cm^{-2}) was about 3.3 times as that of pure m-BWO (0.075 μA cm^{-2}), and about 2.2 times as that of ug-CN (0.12 μA cm^{-2}). The results demonstrated that UTCB-25 possessed higher separation efficiency of photogenerated electron-hole pairs and a lower recombination rate of charge carriers. The superior photoelectric reproducibility of UTCB-25 will greatly exploited its potential application in other fields, such as photodetector, solar cell, and so on.

3.3.2. Roles of reactive species

In order to evaluate the main active species generated during the photocatalytic removal of IBF, three scavengers, benzoquinone (BQ, 2 mM), isopropanol (IPA, 10 mM), and ethylenediamine tetra acetic acid disodium salt (EDTA-Na_2, 10 mM) were added in the photodegradation of IBF as quenchers of •O_2^- radical, •OH radical, and h^+, respectively. As shown in Fig. 10b, the photocatalytic degradation of IBF was significantly inhibited by adding EDTA-Na_2 and weakly hindered after addition of BQ. It is demonstrated that h^+ was the most critical species and •O_2^- served as a secondary active species during the whole degradation reaction. IPA quencher had a slight influence on the degradation rate of IBF during the whole degradation process, implying that •OH radical was not the main reactive species responsible for IBF degradation. The spin-trapping ESR technique was employed to further confirm the roles of reactive species in depth during the photocatalytic process. As shown in Fig. 10c, the characteristic peaks of DMPO-•O_2^- were obviously observed in BQ dispersion of UTCB-25 under visible light irradiation. However, in Fig. 10d, the characteristic peaks corresponding to the DMPO-•OH adduct did not clearly show up even under the visible light irradiation. The ESR results indicate that the •O_2^- radicals were produced during the photocatalytic reaction, while only few •OH radicals could be generated in this system, which are consistent with the above active species trapping experimental results.

3.3.3. Mechanisms of enhanced photocatalytic performance

Based on above results, the photocatalytic mechanism of UTCB-25 heterojunction can be illustrated in Scheme 1. Since the holes are photogenerated directly on the open surface $[BiO]^+$ layers and the electrons are photogenerated in the middle $[WO_4]^{2-}$ layers. It has been demonstrated by DFT (Scheme 1a). The band structure matching was also proved by the XPS VB spectra. On one hand, the holes photogenerated on the upside surface $[BiO]^+$ layers directly react with IBF and oxidize H_2O to form •OH. Simultaneously, the holes photogenerated on the downside surface $[BiO]^+$ layers transfer to the ug-CN surface then react with IBF. On the other hand, the photoelectrons are formed in the middle $[WO_4]^{2-}$ layers where they transfer to the edge of monolayers for reduction reactions. The photogenerated electrons (e^-) in the ug-CN nanosheets tend to transfer to m-BWO [50]. The e^- accumulated in the CB of atomic scale m-BWO could still react with the adsorbed O_2 to generate •O_2^- radicals [27]. The active species of •O_2^- radicals and •OH radicals could continuously decompose IBF. The above procedure was given in Scheme 1b. The interaction of m-BWO and ug-CN enhanced the separation and transfer efficiency of photogenerated carriers, and then further improving the photocatalytic activity. Noticeably, it is in great agreement with the results of the photocurrent analysis. According to the result of main oxidative species detection, the h^+ of ug-CN valance band could degrade IBF directly. Therefore, it could be concluded that the construction of atomic scale UTCB heterojunctions facilitates the efficient separation of photogenerated electron-hole pairs and thus accelerates the process of photocatalytic reaction.

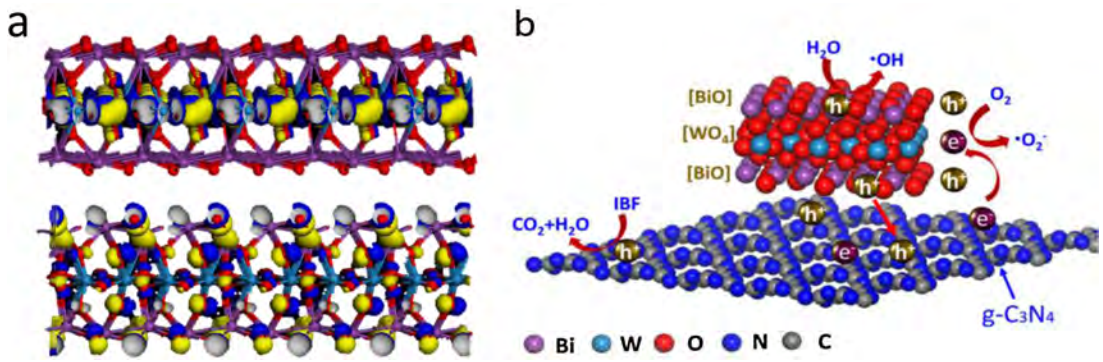

Scheme 1. a) The LUMO (top) and HOMO (bottom) states of the monolayer Bi_2WO_6 nanosheets; b) Photocatalytic mechanism scheme of UTCB heterojunctions under visible light irradiation (>420 nm).

4. Conclusion

In this study, we have successfully constructed an atomic scale 2D-2D heterostructure by introducing monolayer Bi_2WO_6 nanosheets on ultrathin g-C_3N_4 nanosheets through hydrothermal reaction. HR-TEM and AFM revealed that an intimate interface between ug-CN and m-BWO formed in the ultrathin heterojunction. The UTCB-25 showed the optimal efficiency of IBF degradation which reached about 96.1% within 1 h under visible light irradiation, and its degradation rate constant was about 2.7 times as that of pure m-BWO. The photocurrent intensity suggested that the UTCB-25 heterojunction owned an efficient separation rate of photogenerated electron-carriers. The formation of ultrathin heterojunctions with effective charge transfer across substantial heterojunction interface was the main factor contributing to the enhancement of photocatalytic activity for UTCB heterojunctions under visible light irradiation. Quenching experiments indicated that the h^+ was the primary reactive species for the photocatalytic removal of IBF. According to the LC–MS/MS, five possible degradation pathways were proposed, and the direct decarboxylation might be the main degradation pathway of IBF. Our present work provides a new insight on atomic scale 2D/2D heterojunction photocatalysts with effective charge separation for the efficient photodegradation of organic pollutants from wastewater.

Acknowledgements

The study was financially supported by Projects 51579096, 51521006, 51222805, 51679084, 51508175 and 51409024 supported by National Natural Science Foundation of China, the National Program for Support of Top–Notch Young Professionals of China (2012), and the Program for New Century Excellent Talents in University from the Ministry of Education of China (NCET-11-0129).

Appendix A. Supplementary data

Supplementary data associated with this article can be found, in the online version, at http://dx.doi.org/10.1016/j.apcatb.2017.03.019.

References

[1] B. Halling-Sørensen, S.N. Nielsen, P. Lanzky, F. Ingerslev, H.H. Lützhøft, S. Jørgensen, Chemosphere 36 (1998) 357–393.
[2] L. Tang, G.M. Zeng, G.L. Shen, Y.P. Li, Y. Zhang, D.L. Huang, Environ. Sci. Technol. 42 (2008) 1207–1212.
[3] G.P. Anipsitakis, D.D. Dionysiou, Environ. Sci. Technol. 38 (2004) 3705–3712.
[4] Y. Deng, L. Tang, G. Zeng, Z. Zhu, M. Yan, Y. Zhou, J. Wang, Y. Liu, J. Wang, Appl. Catal. B: Environ. 203 (2017) 343–354.
[5] L. Tang, Y.C. Deng, G.M. Zeng, W. Hu, J.J. Wang, Y.Y. Zhou, J.J. Wang, J. Tang, W. Fang, J. Alloy Compd. 662 (2016) 516–527.
[6] H. Shi, G. Chen, C. Zhang, Z. Zou, ACS Catal. 4 (2014) 3637–3643.
[7] A. Fujishima, K. Hashimoto, T. Watanabe, BKC Incorporated, 1999.
[8] Y. Ma, X. Wang, Y. Jia, X. Chen, H. Han, C. Li, Chem. Rev. 114 (2014) 9987–10043.
[9] Y. Sun, S. Gao, F. Lei, Y. Xie, Chem. Soc. Rev. 44 (2015) 623–636.
[10] M. Zhou, X.W. Lou, Y. Xie, Nano Today 8 (2013) 598–618.
[11] U. Maitra, U. Gupta, M. De, R. Datta, A. Govindaraj, C.N.R. Rao, Angew. Chem. Int. Ed. 52 (2013) 13057–13061.
[12] S. Ida, T. Ishihara, J. Phys. Chem. Lett. 5 (2014) 2533–2542.
[13] L. Liang, F. Lei, S. Gao, Y. Sun, X. Jiao, J. Wu, S. Qamar, Y. Xie, Angew. Chem. Int. Ed. 54 (2015) 13971–13974.
[14] D. Voiry, M. Salehi, R. Silva, T. Fujita, M.W. Chen, T. Asefa, V.B. Shenoy, G. Eda, M. Chhowalla, Nano Lett. 13 (2013) 6222–6227.
[15] P. Niu, L. Zhang, G. Liu, H.M. Cheng, Adv. Funct. Mater. 22 (2012) 4763–4770.
[16] Z. Zhang, J. Huang, M. Zhang, Q. Yuan, B. Dong, Appl. Catal. B: Environ. 163 (2015) 298–305.
[17] J. Di, J. Xia, M. Ji, H. Li, H. Xu, H. Li, R. Chen, Nanoscale 7 (2015) 11433–11443.
[18] J. Yang, X. Wang, X. Zhao, J. Dai, S. Mo, J. Phys. Chem. C 119 (2015) 3068–3078.
[19] D. Jiang, T. Wang, Q. Xu, D. Li, S. Meng, M. Chen, Appl. Catal. B: Environ. 201 (2017) 617–628.
[20] Y. Zhou, X. Zhang, Q. Zhang, F. Dong, F. Wang, Z. Xiong, J. Mater. Chem. A 2 (2014) 16623–16631.
[21] S. Ma, J. Xie, J. Wen, K. He, X. Li, W. Liu, X. Zhang, Appl. Surf. Sci. 391 (2017) 580–591.
[22] F. Dong, T. Xiong, Y. Sun, Y. Zhang, Y. Zhou, Chem. Commun. 51 (2015) 8249–8252.
[23] L. Tang, J. Wang, G. Zeng, Y. Liu, Y. Deng, Y. Zhou, J. Tang, J. Wang, Z. Guo, J. Hazard. Mater. 306 (2016) 295–304.
[24] J. Wang, L. Tang, G. Zeng, Y. Liu, Y. Zhou, Y. Deng, J. Wang, B. Peng, ACS Sustain. Chem. Eng. 5 (2017) 1062–1072.
[25] X. Qian, D. Yue, Z. Tian, M. Reng, Y. Zhu, M. Kan, T. Zhang, Y. Zhao, Appl. Catal. B: Environ. 193 (2016) 16–21.
[26] M. Qamar, R.B. Elsayed, K.R. Alhooshani, M.I. Ahmed, D.W. Bahnemann, ACS Appl. Mater. Interfaces 7 (2015) 1257–1269.
[27] Y.G. Zhou, Y.F. Zhang, M.S. Lin, J.L. Long, Z.Z. Zhang, H.X. Lin, J.C.S. Wu, X.X. Wang, Nat. Commun. 6 (2015) 8340.
[28] Y. Zheng, J. Liu, J. Liang, M. Jaroniec, S.Z. Qiao, Energy Environ. Sci. 5 (2012) 6717–6731.
[29] Y.C. Deng, L. Tang, G.M. Zeng, J.J. Wang, Y.Y. Zhou, J.J. Wang, J. Tang, Y. Liu, B. Peng, F. Chen, J. Mol. Catal. a-Chem. 421 (2016) 209–221.
[30] W. Wang, J.C. Yu, D. Xia, P.K. Wong, Y. Li, Environ. Sci. Technol. 47 (2013) 8724–8732.
[31] F. Dong, Z. Zhao, Y. Sun, Y. Zhang, S. Yan, Z. Wu, Environ. Sci. Technol. 49 (2015) 12432–12440.
[32] J.-M. Brozinski, M. Lahti, A. Meierjohann, A. Oikari, L. Kronberg, Environ. Sci. Technol. 47 (2012) 342–348.
[33] H. Dong, G. Zeng, L. Tang, C. Fan, C. Zhang, X. He, Y. He, Water Res. 79 (2015) 128–146.
[34] D.W. Kolpin, E.T. Furlong, M.T. Meyer, E.M. Thurman, S.D. Zaugg, L.B. Barber, H.T. Buxton, Environ. Sci. Technol. 36 (2002) 1202–1211.
[35] T. Heberer, Toxicol. Lett. 131 (2002) 5–17.
[36] F.J. Rivas, F.J. Beltran, J. Frades, P. Buxeda, Water Res. 35 (2001) 387–396.
[37] N. Veldhoen, R.C. Skirrow, L.L. Brown, G. van Aggelen, C.C. Helbing, Environ. Sci. Technol. 48 (2014) 10439–10447.
[38] C.Y. Liu, H.W. Huang, X. Du, T.R. Zhang, N. Tian, Y.X. Guo, Y.H. Zhang, J. Phys. Chem. C 119 (2015) 17156–17165.
[39] J. Li, G.M. Zhan, Y. Yu, L.Z. Zhang, Nat. Commun. 7 (2016).
[40] Y. Zhu, Y. Wang, Q. Ling, Y. Zhu, Appl. Catal. B: Environ. 200 (2017) 222–229.
[41] J.H. Liu, T.K. Zhang, Z.C. Wang, G. Dawson, W. Chen, J. Mater. Chem. 21 (2011) 14398–14401.
[42] K.S.W. Sing, Pure Appl. Chem. 57 (4) (1985) 603–619.
[43] M. Pelaez, A.A. de la Cruz, K. O'shea, P. Falaras, D.D. Dionysiou, Water Res. 45 (2011) 3787–3796.
[44] D. Xia, I.M. Lo, Water Res. 100 (2016) 393–404.

[45] I. Michael, L. Rizzo, C.S. McArdell, C.M. Manaia, C. Merlin, T. Schwartz, C. Dagot, D. Fatta-Kassinos, Water Res. 47 (2013) 957–995.
[46] X.F. Zhou, C. Hu, X.X. Hu, T.W. Peng, J.H. Qu, J. Phys. Chem. C 114 (2010) 2746–2750.
[47] C. Wang, L. Zhu, M. Wei, P. Chen, G. Shan, Water Res. 46 (2012) 845–853.
[48] F. Mendez-Arriaga, S. Esplugas, J. Gimenez, Water Res. 42 (2008) 585–594.
[49] X. Li, Y.J. Wang, S. Yuan, Z.X. Li, B. Wang, J. Huang, S.B. Deng, G. Yu, Water Res. 63 (2014) 81–93.
[50] Y.J. Wang, X.J. Bai, C.S. Pan, J. He, Y.F. Zhu, J. Mater. Chem. 22 (2012) 11568–11573.